

# Stability of Tin- versus Lead-Halide Perovskites: Ab Initio Molecular Dynamics Simulations of Perovskite/Water Interfaces

Waldemar Kaiser,\* Damiano Ricciarelli, Edoardo Mosconi, Asma A. Allothman, Francesco Ambrosio,\* and Filippo De Angelis



Cite This: *J. Phys. Chem. Lett.* 2022, 13, 2321–2329



Read Online

ACCESS |



Metrics & More

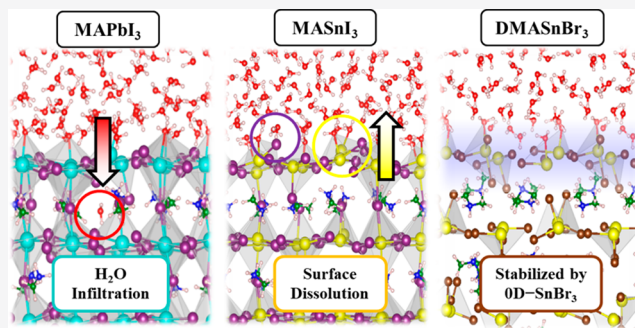


Article Recommendations



Supporting Information

**ABSTRACT:** Tin-halide perovskites (THPs) have emerged as promising lead-free perovskites for photovoltaics and photocatalysis applications but still fall short in terms of stability and efficiency with respect to their lead-based counterpart. A detailed understanding of the degradation mechanism of THPs in a water environment is missing. This Letter presents *ab initio* molecular dynamics (AIMD) simulations to unravel atomistic details of THP/water interfaces comparing methylammonium tin iodide,  $\text{MASnI}_3$ , with the lead-based  $\text{MAPbI}_3$ . Our results reveal facile solvation of surface tin–iodine bonds in  $\text{MASnI}_3$ , while  $\text{MAPbI}_3$  remains more robust to degradation despite a larger amount of adsorbed water molecules. Additional AIMD simulations on dimethylammonium tin bromide,  $\text{DMASnBr}_3$ , investigate the origins of their unprecedented water stability. Our results indicate the presence of amorphous surface layers of hydrated zero-dimensional  $\text{SnBr}_3$  complexes which may protect the inner structure from degradation and explain their success as photocatalysts. We believe that the atomistic details of the mechanisms affecting THP (in-)stability may inspire new strategies to stabilize THPs.



Metal halide perovskites belong to the most promising semiconducting materials for energy conversion from renewable sources in the form of photovoltaics<sup>1</sup> and photocatalysis<sup>2</sup> thanks to their favorable optoelectronic properties, such as direct and tunable band gaps,<sup>3</sup> fast charge transport,<sup>4</sup> low nonradiative recombination,<sup>5</sup> and low-temperature processing capabilities from solution.<sup>6</sup> Thin film solar cells based on lead-halide perovskites (LHPs) have recently reached 25.2% efficiency with significant long-term stability,<sup>7</sup> rivaling silicon solar cells.

A tremendous drawback which may limit the industrial market potential of state-of-the-art perovskite photovoltaics is the presence of lead in the B-site of the  $\text{ABX}_3$  perovskite crystal structure. Recent reports<sup>8,9</sup> have underlined the detrimental impact of lead on the environment and human health, and have further raised the need for lead-free alternatives. Tin-halide perovskites (THPs) have emerged as one of the most promising lead-free alternative for photovoltaics<sup>10–12</sup> with record efficiencies of 14.6%<sup>13</sup> in pure THPs and beyond 20% in mixed tin–lead perovskites.<sup>14–17</sup> Despite having an optimal band gap ( $\sim 1.2$ – $1.3$  eV) for photovoltaic applications, THP performance and stability are still behind their lead-based counterpart. One of the critical aspects limiting the performance and the stability of THPs is the facile oxidation of Sn(II) to Sn(IV),<sup>18,19</sup> which may induce a large self-p-doping in the perovskite bulk and deep electron trap states at the perovskite surface.<sup>20–22</sup> Experimental reports demonstrate THPs degra-

degradation even in well-encapsulated thin films under exposure of light or under elevated temperatures.<sup>23–25</sup>

Understanding of the perovskite (in-)stability and associated degradation mechanisms is of utmost importance to achieve reliable and long-term stable THPs. Previous studies have shed light on the degradation of the lead-based counterpart, methylammonium lead iodide,  $\text{MAPbI}_3$ . *Ab initio* molecular dynamics (AIMD) simulations<sup>26</sup> were reported on the degradation of MAI-terminated surfaces by a rapid solvation process which occurs by the bonding of water molecules to the Pb atoms with subsequent release of surface iodine atoms. Metadynamics simulations showed that, after the initial Pb–I bond breaking, further hydration of iodine provides the required energy to overcome the  $\text{I}^-$ - $\text{MA}^+$  attraction.<sup>27</sup> On the contrary, the  $\text{PbI}$ -terminated surface is more robust to degradation, while water molecules may enter into the  $\text{MAPbI}_3$  bulk and form intermediate hydrated phases,<sup>26,28,29</sup> which is a key step of perovskite degradation upon water exposure.<sup>30–32</sup> Water-intercalated  $\text{MAPbI}_3$  readily forms  $\text{PbI}_2$  vacancy

Received: January 27, 2022

Accepted: February 28, 2022

complexes and induces electronic trap states.<sup>33</sup> The presence of water can be both detrimental or beneficial to the excited state lifetime, depending on the level of humidity exposure.<sup>34</sup> Light exposure can further drive perovskite degradation by dissociating water molecules to  $\text{OH}^-$ , which may deprotonate the MA cation followed by desorption of  $\text{CH}_3\text{NH}_2$ .<sup>35–37</sup> Interestingly, partial replacement of iodine with bromine can enhance perovskite stability toward water and oxygen.<sup>37,38</sup>

Recent studies connected the degradation of THPs with the release of  $\text{SnO}_2$  and  $\text{SnI}_4$ , while in mixed tin-lead perovskites  $\text{I}_2$  formation also was observed.<sup>24</sup> The presence of oxygen and moisture further accelerates THP degradation by formation of  $\text{SnI}_4$ .<sup>39,40</sup> Density functional theory (DFT) simulations suggest that adsorbed water or oxygen, by formation of H–I or Sn–O bonds, strongly affects the Sn–I bonds at the methylammonium tin iodide,  $\text{MASnI}_3$ , surface,<sup>39,41</sup> which is less significant in the case of  $\text{MAPbI}_3$ .<sup>41</sup> The presence of water molecules in THPs may further reduce light absorption and lead to faster charge relaxation.<sup>42</sup> Several strategies such as metal doping,<sup>43</sup> Lewis-base post-treatment,<sup>44</sup> or capping 3D THP with analogue 2D large-cation perovskites<sup>45</sup> were proposed to mitigate tin oxidation, which in turn may stabilize THPs.

Despite recent efforts, a clear mechanistic picture of the factors affecting THP stability in a water environment is still missing. Here we report comparative AIMD simulations of  $\text{MASnI}_3$  with the prototypical lead-based  $\text{MAPbI}_3$  perovskite, Figure 1a,b, thus assessing the impact of the B-site metal on

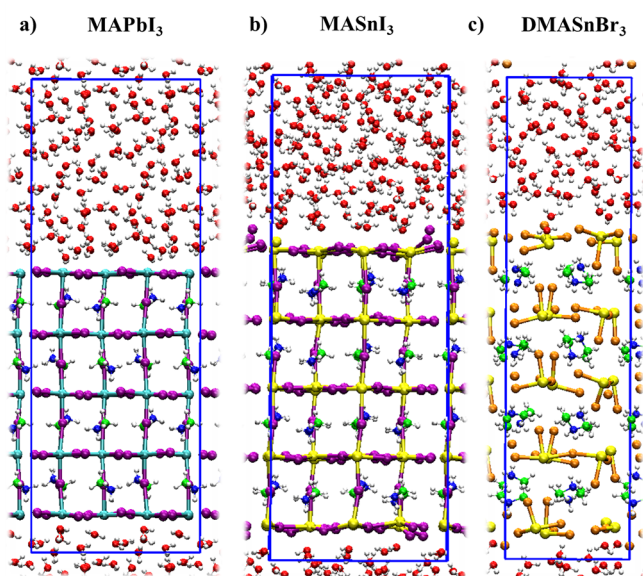


**Figure 1.** Structural model of the (a)  $\text{MAPbI}_3$ , (b)  $\text{MASnI}_3$ , and (c)  $\text{DMASnBr}_3$  perovskite/water interfaces. The colors of the atoms are cyan: Pb, yellow: Sn, purple: I, orange: Br, green: C, white: H, blue: N, red: O. Further details on the structural models are provided in the Computational Details.

the interaction with water. A comparison with dimethylammonium tin bromide,  $\text{DMASnBr}_3$ , Figure 1c, a water-stable perovskite catalyst,<sup>46</sup> is also reported, which allows us to comparatively evaluate the concomitant impact of the A-site and X-site variation on the perovskite/water interface stability. Note that AIMD results on the water-induced degradation of  $\text{MAPbI}_3$  are partially reproduced from our previous analysis,<sup>26</sup> together with additional statistical analysis, to provide a direct

comparison with the prototypical  $\text{MAPbI}_3$ /water interface as representative of the lead-based counterpart. Our results reveal a dissolution of the  $\text{SnI}_2$ -terminated  $\text{MASnI}_3$  surface under water which is initiated by the formation of Sn–O bonds and the subsequent breaking of axial Sn–I bonds. The  $\text{MAPbI}_3$  surface, despite showing an increased amount of adsorbed water molecules, preserves its inorganic Pb–I framework without a substantial difference in the radial pair distribution between bulk and surface. However, water infiltration is observed, which presents the first step of  $\text{MAPbI}_3$  degradation. Our results indicate that the high water stability of  $\text{DMASnBr}_3$  is due to the presence of an amorphous surface layer made of disconnected, zero-dimensional  $\text{SnBr}_3$  complexes, stabilized by strong Sn–Br bonds, which strongly bind water molecules and protect the  $\text{DMASnBr}_3$  bulk.

We start our analysis by comparing the interaction of the (001)  $\text{MI}_2$ -terminated ( $M = \text{Pb}, \text{Sn}$ ) tetragonal  $\text{MAPbI}_3$  and  $\text{MASnI}_3$  perovskite surfaces with the surrounding liquid water environment (see Computational Details for model setup and AIMD simulation details). The (001) surface belongs to the most stable perovskite surfaces<sup>47</sup> and has been subject to several studies on the electronic properties of lead-<sup>26,28,32</sup> and tin-based perovskites.<sup>21,22,39,45</sup> The radial pair distribution function  $g^{M-O}(r)$  ( $M = \text{Sn}, \text{Pb}$ ), averaged over the AIMD trajectories, indicates a strong interaction of the Sn surface atoms with the water oxygen atoms, as shown by the peak located at 2.43 Å; see Figure 2a. The  $g^{\text{Pb-O}}(r)$  of the  $\text{MAPbI}_3$  surface comparatively shows a substantially broadened peak

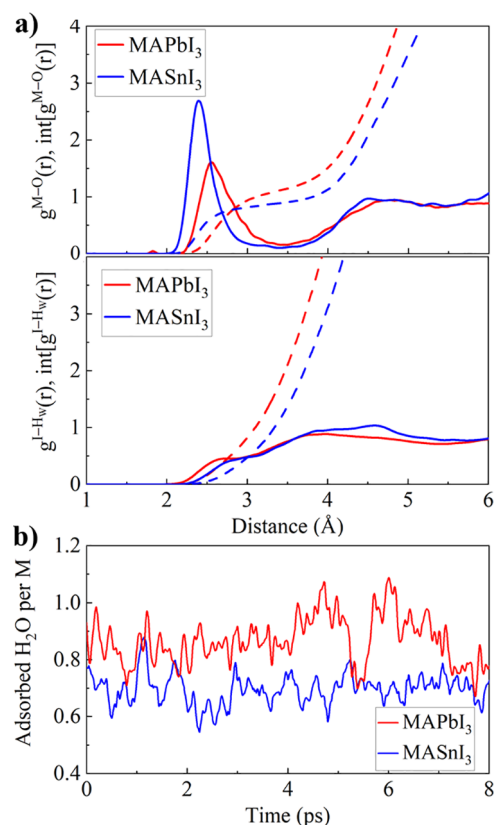


**Figure 2.** (a) M–O ( $M = \text{Sn}, \text{Pb}$ ) and I– $\text{H}_w$  radial pair distribution,  $g^{M-O}(r)$  and  $g^{I-Hw}(r)$ , and the integrated distribution,  $\text{int}[g^{M-O}(r)]$  and  $\text{int}[g^{I-Hw}(r)]$ , for  $\text{MAPbI}_3$  (red) and  $\text{MASnI}_3$  (blue). (b) Time evolution of the number of adsorbed  $\text{H}_2\text{O}$  molecules per surface metal atom, identified by M–O bonds below 3.0 Å.

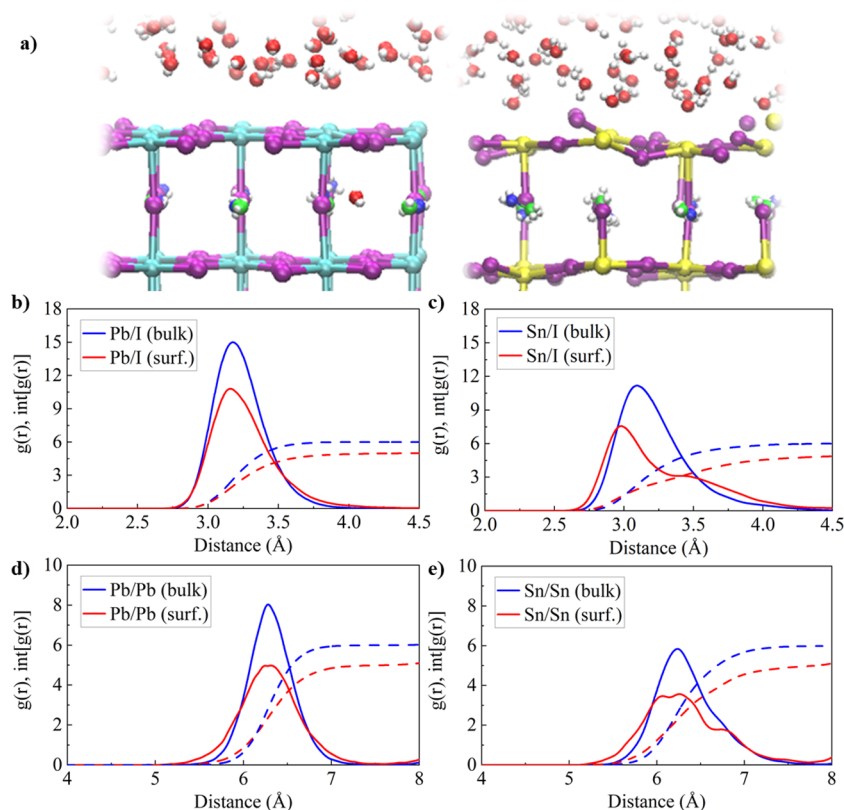


**Figure 3.** (a) Time-averaged structure for (left) MAPbI<sub>3</sub>/water and (right) MASnI<sub>3</sub>/water interface. Panels (b) and (c) give the Pb/I and Sn/I radial pair distribution,  $g(r)$  (solid), and the integrated distribution,  $\text{int}[g(r)]$  (dashed), for MAPbI<sub>3</sub> and MASnI<sub>3</sub>, respectively. Panels (d) and (e) give the Pb/Pb and Sn/Sn  $g(r)$  (solid) and  $\text{int}[g(r)]$  (dashed) for MAPbI<sub>3</sub> and MASnI<sub>3</sub>, respectively. In (c–e), we distinguish between the surface, defined by the outermost MI<sub>2</sub> layers (M = Sn, Pb), and the bulk, defined by the inner layers. The notation, e.g., Sn/I (surf.), represents the  $g(r)$  of surface Sn atoms with all (surface and bulk) I atoms.

centered at around 2.53 Å. The interaction at the perovskite/water interface mainly occurs via the O lone pair electrons and the M<sup>2+</sup> metal atoms forming M–O bonds (M = Sn, Pb), while the contribution of I–H<sub>w</sub> bonds between the surface iodine atoms and the water hydrogen atoms is less pronounced, Figure 2a. Fitting the tail of the  $g^{I-H_w}(r)$  at low distances with a Gaussian distribution, we may estimate an average I–H<sub>w</sub> bond distance of 2.73 Å for MAPbI<sub>3</sub> and 2.91 Å for MASnI<sub>3</sub>, indicating a stronger interaction at the MAPbI<sub>3</sub>/water interface. Both perovskite slabs show a lack of long-range correlation between the surface atoms and the water environment. Note that, within feasible AIMD time scales, the interaction of the perovskite slabs and the water environment mainly occurs at the surface, as visible in the M/O (M = Sn, Pb)  $g(r)$  in Figure S1, Supporting Information. Despite the pronounced Sn–O bond structure, the amount of water molecules adsorbed at the perovskite surface via M–O bonds is higher for MAPbI<sub>3</sub>, on average  $0.88 \pm 0.09$  adsorbed water molecules per surface Pb compared to  $0.69 \pm 0.05$  adsorbed water molecules per surface Sn atom, Figure 2b. Previous DFT studies<sup>48</sup> showed a substantial increase in the ionic contribution to the M–O and I–H<sub>w</sub> bonds at the PbI<sub>2</sub>-terminated MAPbI<sub>3</sub> surface compared to the SnI<sub>2</sub>-terminated MASnI<sub>3</sub> surface. This should lead to an increased attraction of the water oxygen atoms at the MAPbI<sub>3</sub> surface and may explain the  $g^{I-H_w}(r)$  shift toward lower distances, Figure 2a, and finally in the increased number of adsorbed water molecules at the MAPbI<sub>3</sub> surface.

We now move on to study the structural properties at the hydrated perovskite surfaces and bulk for MAPbI<sub>3</sub> and MASnI<sub>3</sub>. We observe substantial differences in the surface structure when considering the time average for each atom over the AIMD trajectory, Figure 3a. Surprisingly, despite the substantial interaction of the MAPbI<sub>3</sub> surface atoms with the water environment, the time-averaged MAPbI<sub>3</sub> surface seems only weakly distorted. In contrast, the MASnI<sub>3</sub> surface shows a strong structural distortion in the inorganic Sn–I framework and indicates broken Sn–I bonds in the surface planes and in between the layers. In the time-averaged MAPbI<sub>3</sub>/water interface, we observe a water molecule which has entered the MAPbI<sub>3</sub> bulk being located in the first MAI layer, as reported in our previous study.<sup>26</sup>

To quantify these visual observations, we compare the radial pair distributions for the individual components in both MAPbI<sub>3</sub> and MASnI<sub>3</sub>. Note that we distinguish between surface atoms, given by the atoms located within the outer PbI<sub>2</sub> and SnI<sub>2</sub> layers, and identify the remaining atoms as bulk. The Pb/I bulk  $g(r)$ , Figure 3b, shows a sharp peak at 3.17 Å, being near the experimental bond Pb–I length of  $\sim 3.19$  Å,<sup>49</sup> and its integral reaches the expected coordination number of 6 within 3.8 Å. At the surface, the peak is shifted to 3.14 Å and slightly broadened; the Pb/I coordination number of surface Pb atoms reaches the expected value of 5 within 4.1 Å. The bulk and surface Pb/Pb  $g(r)$  both reach the maximum at 6.30 Å, while the surface Pb/Pb  $g(r)$  is slightly broadened, Figure 3d. Unlike for MAPbI<sub>3</sub>, we observe substantial differences between the surface and the bulk  $g(r)$  for MASnI<sub>3</sub>. The bulk Sn/I  $g(r)$ ,

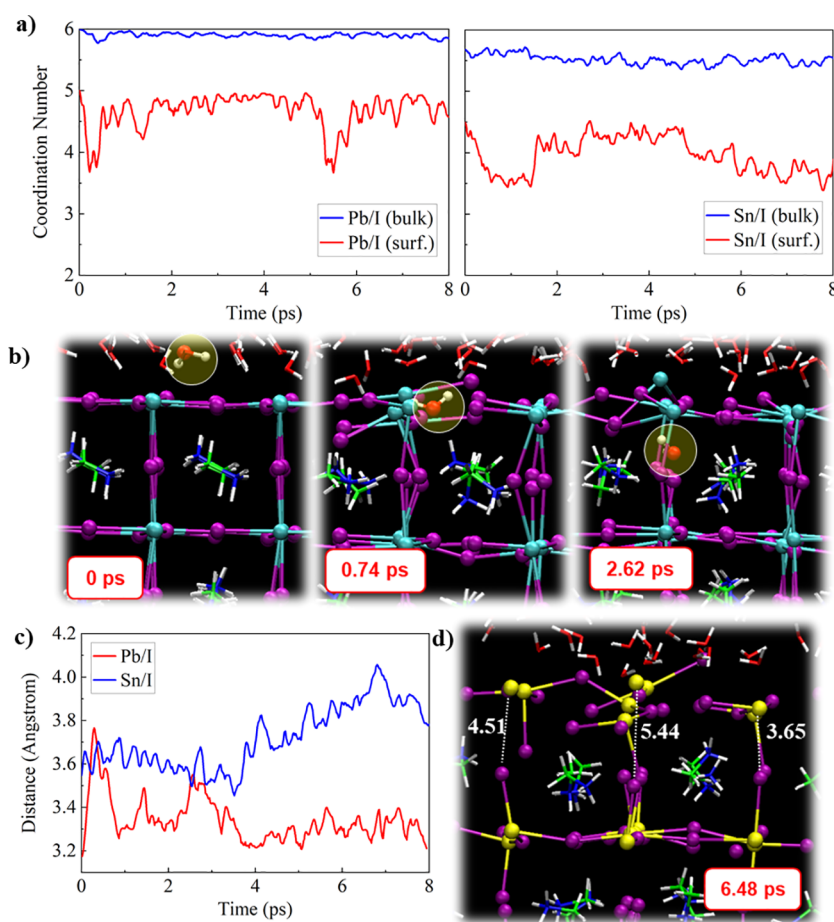


**Figure 4.** (a) Time evolution of the (left) Pb/I and (right) Sn/I coordination number in the bulk and at the surface. (b) Key steps of the infiltration of the water molecule into the MAPbI<sub>3</sub> slab. (c) Time evolution of the average interlayer distance between the surface metal atoms and the iodine atoms in the first MAI layer. (d) Structure visualizing the dissolution of the MASnI<sub>3</sub> surface; interlayer distances are given for several Sn–I pairs, in units of Angstrom.

Figure 3c, is substantially broadened with a maximum at 3.07 Å, and the  $\text{int}[g(r)]$  reaches the expected Sn/I coordination number of 6 within 4.31 Å; surface Sn/I  $g(r)$  substantially differs from the bulk and shows a sharp peak at 2.99 Å, representing the equatorial Sn–I bonds, and a broadened contribution at large distances centered at around 3.48 Å, representing the axial Sn–I bonds between surface Sn and I from the first MAI layer. The Sn/I coordination number slowly increases with distance and reaches the expected value of 5 after 5.11 Å, which clearly points to elongated and potentially even broken bonds as observed in Figure 3a. The interaction of the water environment with the MASnI<sub>3</sub> surface further broadens the surface Sn/Sn  $g(r)$ , Figure 3e, while the bulk Sn/Sn  $g(r)$  remains at the expected Sn–Sn distance of 6.21 Å. Interestingly, the I/I  $g(r)$  do not show substantial differences between the hydrated surfaces and the bulk for both of the considered perovskites, Figure S2, Supporting Information.

It is also interesting to investigate the structural properties of the MA cations in terms of the metal/MA  $g(r)$  and the orientation of the MA within the inorganic cages. The apparent stability of the MAPbI<sub>3</sub> surface is also reflected in the Pb/MA  $g(r)$ , Figure S2c, Supporting Information. We observe a broad distribution for both the bulk and the surface, which, however, follow the same shape. In contrast, the Sn/MA  $g(r)$  of the surface Sn atoms varies from the bulk and shows a flattened distribution, which indicates a lack of correlation between the

surface Sn atoms and the MA cations. Interestingly, the MA cations in the MAI layers near the SnI<sub>2</sub>-terminated surface are highly oriented at  $\pm 30^\circ$  (layer 1 and layer 4 in Figure S3b, Supporting Information), while MA orientation in the hydrated MAPbI<sub>3</sub> is strongly perturbed in comparison to the bare MAPbI<sub>3</sub> slabs.<sup>26</sup> Despite the strong structural disorder in the hydrated MASnI<sub>3</sub> surface, the I/MA  $g(r)$  of surface I atoms follows the bulk  $g(r)$  closely, Figure S2f, Supporting Information, which may explain the high orientation of the MA cations in MASnI<sub>3</sub>.

To establish the main water-induced degradation mechanism of the MASnI<sub>3</sub> surface, we now analyze the temporal evolution of the surface bonds in terms of the Sn/I coordination number in comparison to MAPbI<sub>3</sub>, Figure 4a. The Pb/I coordination number in the MAPbI<sub>3</sub> bulk remains close to 6 throughout the trajectory; at the surface, it remains approximately 5 until 5.2 ps and then drops to  $\sim 3.5$  for a short time. This is caused by a breaking of equatorial Pb–I bonds at the hydrated surface, while the axial Pb–I bonds between the surface and the first MAI layer remain stable, Figure S4, Supporting Information. The equatorial Pb–I bonds, however, are restored after a short time period such that the coordination number approaches a value of 5 again. As shown in our previous study, the fundamental degradation mechanism of the MAPbI<sub>3</sub> surface is initiated by the infiltration of the water molecule,<sup>26</sup> Figure 4b. Recent classical

molecular dynamics simulations underlined that water infiltration into the perovskite bulk is a crucial step to initiate the degradation of  $\text{PbI}_2$ -terminated surfaces.<sup>32</sup> Within the AIMD trajectory, we did not observe the infiltration of water molecules for the  $\text{MASnI}_3$  surface. The Sn/I coordination number of the surface Sn decreases slowly in time from  $\sim 4.5$  after the thermalization period (first  $\sim 2$  ps) to  $\sim 3.5$  at 8 ps, Figure 4a. The origin of this change in coordination number is the breaking of axial bonds between the surface Sn atoms and the I atoms in the first MAI layer. The average Sn–I interlayer distance increases from  $\sim 3.5$  Å at 3.7 ps to a maximum of  $\sim 4.0$  Å at 6.8 ps, Figure 4c, while individual Sn–I distances above 5.4 Å can be observed, Figure 4d. In contrast, the Pb–I interlayer distance remains stable at around 3.2 Å as the main effect of the water is on the equatorial Pb–I bonds, without strongly changing the axial Pb–I bonds.

The presented observations give clear indication of a *facile solvation of the  $\text{SnI}_2$ -terminated surface by water*. As a consequence, we may expect an enhanced surface defect density in humid conditions which can introduce deep trap states and strongly suppresses the device performance of THP solar cells.<sup>21</sup> On a longer time scale, water may easily enter the  $\text{MASnI}_3$  bulk through the dissolved surface to accelerate the degradation<sup>32</sup> and hamper the electronic properties.<sup>42</sup> This emphasizes the need for perovskite synthesis under a controlled moisture-free environment and additionally may require passivation of  $\text{MASnI}_3$  using hydrophobic protection layers. Note that we previously observed the rapid solvation of the MAI-terminated  $\text{MAPbI}_3$  surface from AIMD simulations, which occurs by the release of I atoms under the attack of water molecules at Pb sites.<sup>26</sup> Further DFT studies reported comparable water adsorption energies on MAI-terminated  $\text{MAPbI}_3$  and  $\text{MASnI}_3$  surfaces.<sup>48</sup> We thus are confident that the degradation process of the MAI-terminated  $\text{MASnI}_3$  will follow a similar mechanism as in  $\text{MAPbI}_3$ .

We now analyze the results on the (001)  $\text{SnBr}_2$ -terminated orthorhombic  $\text{DMASnBr}_3$ /water interface to gain a deeper understanding of the origin of the high water stability of  $\text{DMASnBr}_3$ .<sup>46,50</sup> The  $g^{\text{Sn-O}}(r)$  of the  $\text{DMASnBr}_3$  surface shows a maximum at 2.37 Å, close to the Sn–O peak of  $\text{MASnI}_3$  (2.43 Å), while the  $g^{\text{Br-H}_w}(r)$  is substantially shifted with respect to  $\text{MASnI}_3$  to shorter distances, Figure 5a. Additionally, the intensity of the  $\text{DMASnBr}_3$   $g^{\text{Sn-O}}(r)$  is less pronounced, which we may attribute to Sn–Br bonds being stronger than Sn–I ones. The overall amount of adsorbed water molecules per surface Sn atom does not substantially vary between the considered THPs, Figure S5, Supporting Information. Furthermore, the  $\text{DMASnBr}_3$   $\text{int}[g(r)]$  follows closely the one of  $\text{MASnI}_3$ , suggesting a comparable interaction of the perovskite surface and water environment. In contrast to the substantial distortion of the Sn–I bonds at the  $\text{MASnI}_3$  surface, however, the Sn/Br  $g(r)$  indicates highly stable metal-halide bonds at the  $\text{DMASnBr}_3$  surface, Figure 5b. Interestingly, the short-range correlation, given by the first peak in the Sn/Br  $g(r)$ , is nicely preserved, but the second peak is flattened, which points to a rather disordered surface structure. Also, the Br/Br  $g(r)$  is preserved at the surfaces, Figure S6, Supporting Information. The Sn/Br coordination number does not strongly change with time, with an average of 3.61 and 2.99 of the bulk and of the surface Sn atoms, respectively, Figure S7, Supporting Information. In contrast to  $\text{MASnI}_3$ , the interlayer distance between the surface Sn atoms and the Br atoms in the first DMAr layer remains relatively stable but shows larger

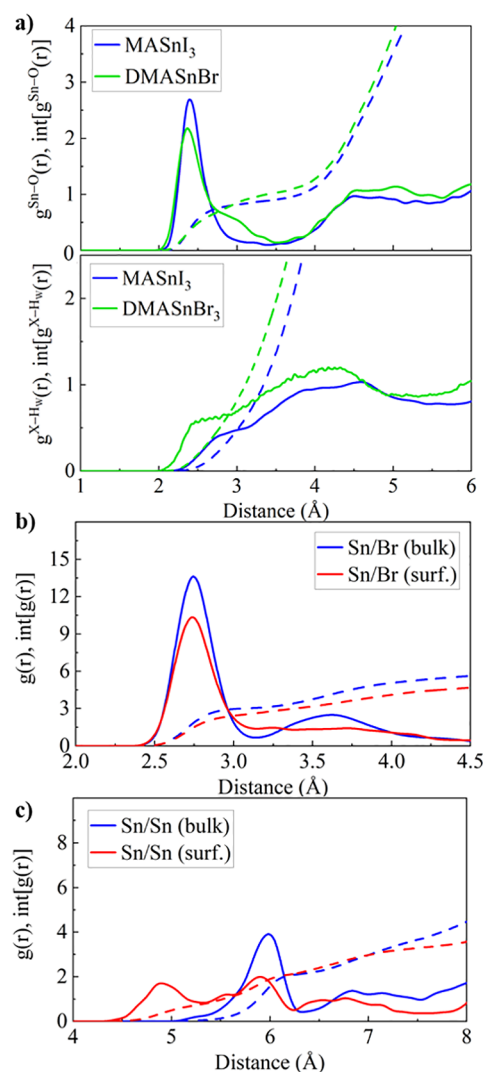


**Figure 5.** (a) Sn–O and X–H<sub>w</sub> (X = Br, I) radial pair distribution and the integrated distribution for  $\text{MASnI}_3$  (blue) and  $\text{DMASnBr}_3$  (green). (b) Sn/Br and (c) Sn/Sn  $g(r)$  of  $\text{DMASnBr}_3$  in the bulk (blue) and at the surface (red).

fluctuations, Figure S8, Supporting Information. The most significant difference to  $\text{MASnI}_3$  is the highly disordered Sn/Sn  $g(r)$  at the  $\text{DMASnBr}_3$  surface, Figure 5c. While the bulk Sn/Sn distribution shows a well-pronounced peak at 5.97 Å, the surface Sn/Sn  $g(r)$  lacks both short- and long-range order. Such a distribution is atypical for a crystalline solid and points to a rather amorphous phase.

Further inspection reveals, indeed, that the  $\text{DMASnBr}_3$  surface consists of disconnected, zero-dimensional  $\text{SnBr}_3$  complexes which form a surface layer possibly protecting the inner bulk structure. Surface Sn atoms form three stable Sn–Br bonds with well-preserved Sn/Br and Br/Br  $g(r)$  and lack of Sn/Sn correlations, which are strong signatures of such 0D- $\text{SnBr}_3$  complexes, Figure S9, Supporting Information. A comparison of the crystal structures of  $\text{DMASnBr}_3$  and  $\text{MASnBr}_3$  (Figure S10, Supporting Information) shows equal Sn–Br bond lengths along the (001) direction for  $\text{MASnBr}_3$  and alternating short ( $\sim 2.74$  Å) and long Sn–Br bonds ( $\sim 3.45$  Å) for  $\text{DMASnBr}_3$ . Consequently, the presence of  $\text{SnBr}_3$  complexes within  $\text{DMASnBr}_3$  can be attributed to the large DMA cation. Recent AIMD simulations also observed the

presence of partially decoupled  $\text{SnBr}_3$  complexes within formamidinium tin bromide,  $\text{FASnBr}_3$ ,<sup>51</sup> which form instantaneously caused by the large size of the FA cation. Water molecules form strong Sn–O bonds with such surface complexes, which is supported by DFT calculations of the water adsorption energy, with  $E_{\text{ads}}(\text{DMASnBr}_3) = -0.72$  eV to  $E_{\text{ads}}(\text{MASnI}_3) = -0.55$  eV, Figure S11, Supporting Information. Relaxing the  $\text{DMASnBr}_3$  slab at  $t = 8$  ps after removal of the water molecules does not lead to a more stable structure, Figure S12, Supporting Information, which indicates that the amorphous surface layer is formed upon interaction with water molecules at finite temperatures. Within the simulated time scales, water molecules neither enter into the perovskite nor are able to dissolve the surface. The OD-SnBr<sub>3</sub> complexes can easily rearrange at the surface to bond with water molecules and consequently to prohibit water from entering the surface. Moreover, the water environment cannot easily break the strong Sn–Br bonds, which limits the solubility of the  $\text{DMASnBr}_3$  surface by water. As a final remark,  $\text{DMASnBr}_3$  is further stabilized by the relatively strong hydrophobic nature of the DMA cation with respect to MA.<sup>46</sup> As a consequence, higher stability of DMA-terminated surfaces compared to  $\text{MASnI}_3$  may be expected due to a reduced solvation of DMA cations, and water infiltration into the  $\text{SnBr}_2$ -terminated  $\text{DMASnBr}_3$  surface may be further suppressed. The high band gap ( $\sim 2.8$  eV<sup>50</sup>) in combination with the amorphous surface layer may prevent the applicability of  $\text{DMASnBr}_3$  in photovoltaics. On the contrary, this inherent surface stability can be the crucial aspect for exploitation of  $\text{DMASnBr}_3$  as water-stable THP in photocatalytic applications.

In summary, we have reported *ab initio* molecular dynamics simulations to investigate the surface degradation of tin-halide perovskites using two prototypical systems, i.e.,  $\text{MASnI}_3$  and  $\text{DMASnBr}_3$ , and provided a comparison with the prototypical lead-based counterpart  $\text{MAPbI}_3$ . Our results show a facile dissolution of the  $\text{SnI}_2$ -terminated  $\text{MASnI}_3$  surface under water. Water molecules bond with the surface Sn atoms and induce the breaking of axial Sn–I bonds with the I atoms of the adjacent MAI layer. Our AIMD results predict a higher water stability of the  $\text{PbI}_2$ -terminated  $\text{MAPbI}_3$  surface. Despite showing an increased number of adsorbed water molecules on the  $\text{MAPbI}_3$  surface, the lead iodine bonds remain stable throughout the trajectory without showing any substantial difference in the radial pair distribution between the bulk and the surface. Still, water molecules may enter the  $\text{MAPbI}_3$  bulk where they may initiate the solvation of the perovskite.<sup>26,32</sup> Finally, we reported AIMD simulations to analyze the origin of the experimentally reported<sup>46,50</sup> surface stability of  $\text{DMASnBr}_3$  in a liquid water environment. We observed highly stable Sn–Br bonds at the surface and an increased stability of the inorganic framework along the  $c$ -axis. Our results show that the  $\text{DMASnBr}_3$  surface is made of disconnected, zero-dimensional  $\text{SnBr}_3$  complexes which form an amorphous layer that can easily reorient within the surface and hereby protect the  $\text{DMASnBr}_3$  bulk. Such amorphous surface structures typically are believed to be detrimental in terms of photovoltaics but may be key for the applicability of THPs in photocatalysis. Overall, we believe that the reported atomistic details of the THP/water interface in this work will inspire novel surface modification and device engineering strategies to enhance the stability of THPs for lead-free perovskite photovoltaics and photocatalysis.

**Computational Details.** The models of the THP–water interfaces are constructed by five  $\text{SnX}_2$  ( $X = \text{I}, \text{Br}$ ) layers such that the perovskite slabs are terminated by  $\text{SnX}_2$  layers, Figure 1. The cell parameters in the  $a$  and  $b$  axes are fixed to the experimental values:  $\text{MASnI}_3$ ,  $a = b = 17.5154$  Å,<sup>52</sup>  $\text{DMASnBr}_3$ ,  $a = 12.274$  Å,  $b = 12.071$  Å,<sup>46</sup> representing  $2 \times 2$  (001) slabs of the tetragonal  $\text{MASnI}_3$  and of the orthorhombic  $\text{DMASnBr}_3$  phases. A vacuum region of 15 Å was added on top of the perovskite slabs, such that  $\text{MASnI}_3$ ,  $c = 47.709$  Å and  $\text{DMASnBr}_3$ ,  $c = 47.5$  Å. The vacuum region was filled by 155 and 72 water molecules for the  $\text{MASnI}_3$  and the  $\text{DMASnBr}_3$  model, respectively, thus giving rise to a liquid water environment characterized by the experimental density of liquid water. We reproduce part of our previous AIMD analysis on the water-induced degradation of  $\text{MAPbI}_3$ ,<sup>26</sup> together with additional statistical analysis, to provide a direct comparison with the prototypical  $\text{MAPbI}_3$ /water interface as representative of the lead-based counterpart.

We carried out AIMD simulations on the THP–water interface models using the Quickstep module in the CP2K software package.<sup>53–56</sup> We used a double- $\zeta$  basis set (DZVP-MOLOPT)<sup>57</sup> combined with the norm-conserving Goedecker–Teter–Hutter (GTH) pseudopotentials<sup>58</sup> and a CUTOFF = 800 Ry, and REL\_CUTOFF = 50 Ry for the expansion of the electron density. The revised PBE (revPBE) parametrization of the PBE functional was used to account for the exchange and correlation potentials. van der Waals corrections are included by means of the rVV10 functional to account for nonlocal electron correlations.<sup>59</sup> The temperature was controlled by a Nosé–Hoover thermostat<sup>60,61</sup> with a target temperature of 350 K and a time constant of 16.68 fs, and the volume was kept constant by applying an NVT ensemble. The integration time step of the dynamics was set to 0.48 fs. The AIMD simulations were run for at least 8 ps for both the  $\text{MASnI}_3$ /water and the  $\text{DMASnBr}_3$ /water interface model.

## ■ ASSOCIATED CONTENT

### Supporting Information

The Supporting Information is available free of charge at <https://pubs.acs.org/doi/10.1021/acs.jpcllett.2c00273>.

Radial pair distribution functions for  $\text{MAPbI}_3$  and  $\text{MASnI}_3$ ; methylammonium orientation in the individual MAI layers; snapshot visualizing the equatorial Pb–I bond breaking at the hydrated  $\text{MAPbI}_3$  surface; time evolution of the adsorbed water molecules at the  $\text{MASnI}_3$  and the  $\text{DMASnBr}_3$  surface; Sn/DMA and Br/Br radial pair distribution functions for  $\text{DMASnBr}_3$ ; AIMD snapshot of the  $\text{DMASnBr}_3$ –water interface visualizing  $\text{SnBr}_3$  complexes; crystal structures of  $\text{MASnI}_3$ ,  $\text{MASnBr}_3$ , and  $\text{DMASnBr}_3$ ; DFT calculations of the adsorption energy of a single water molecule on the perovskite surfaces; optimized  $\text{DMASnBr}_3$  slabs before and after the interaction with water (PDF)

## ■ AUTHOR INFORMATION

### Corresponding Authors

Waldemar Kaiser – Computational Laboratory for Hybrid/Organic Photovoltaics (CLHYO), Istituto CNR di Scienze e Tecnologie Chimiche “Giulio Natta” (CNR-SCITEC), 06123 Perugia, Italy; [orcid.org/0000-0001-9069-690X](https://orcid.org/0000-0001-9069-690X); Email: [waldemar.kaiser@scitec.cnr.it](mailto:waldemar.kaiser@scitec.cnr.it)

**Francesco Ambrosio** – Computational Laboratory for Hybrid/Organic Photovoltaics (CLHYO), Istituto CNR di Scienze e Tecnologie Chimiche “Giulio Natta” (CNR-SCITEC), 06123 Perugia, Italy; Department of Chemistry and Biology “A. Zambelli”, University of Salerno, 84084 Fisciano, Salerno, Italy; CNST@Polimi, Istituto Italiano di Tecnologia, 20133 Milano, Italy; [orcid.org/0000-0002-6388-9586](https://orcid.org/0000-0002-6388-9586); Email: [fambrosio@unisa.it](mailto:fambrosio@unisa.it)

## Authors

**Damiano Ricciarelli** – Computational Laboratory for Hybrid/Organic Photovoltaics (CLHYO), Istituto CNR di Scienze e Tecnologie Chimiche “Giulio Natta” (CNR-SCITEC), 06123 Perugia, Italy; Department of Chemistry, Biology and Biotechnology, University of Perugia, 06123 Perugia, Italy; [orcid.org/0000-0003-4213-2514](https://orcid.org/0000-0003-4213-2514)

**Edoardo Mosconi** – Computational Laboratory for Hybrid/Organic Photovoltaics (CLHYO), Istituto CNR di Scienze e Tecnologie Chimiche “Giulio Natta” (CNR-SCITEC), 06123 Perugia, Italy; Chemistry Department, College of Science, King Saud University, Riyadh 11451, Kingdom of Saudi Arabia; [orcid.org/0000-0001-5075-6664](https://orcid.org/0000-0001-5075-6664)

**Asma A. Alothman** – Chemistry Department, College of Science, King Saud University, Riyadh 11451, Kingdom of Saudi Arabia

**Filippo De Angelis** – Computational Laboratory for Hybrid/Organic Photovoltaics (CLHYO), Istituto CNR di Scienze e Tecnologie Chimiche “Giulio Natta” (CNR-SCITEC), 06123 Perugia, Italy; Department of Chemistry, Biology and Biotechnology, University of Perugia, 06123 Perugia, Italy; [orcid.org/0000-0003-3833-1975](https://orcid.org/0000-0003-3833-1975)

Complete contact information is available at:  
<https://pubs.acs.org/10.1021/acs.jpcllett.2c00273>

## Notes

The authors declare no competing financial interest.

## ACKNOWLEDGMENTS

The Ministero dell’Istruzione dell’Università e della Ricerca (MIUR) and Università degli Studi di Perugia are acknowledged for financial support through the program “Dipartimenti di Eccellenza 2018–2022” (Grant AMIS) to F.D.A. This research was funded by PON Project “Tecnologia per celle solari bifacciali ad alta Efficienza a 4 terminali per utility scale” (BEST-4U) of the Italian Ministry MIUR (CUP B88D19000160005) and by project Ricerca@CNR PHOTOCAT (CUP B93C21000060006). F.A. acknowledges support from by the European Union’s Horizon 2020 research and innovation program under Grant Agreement No 771528 of the SOPHY project. E.M. and A.A.A. wish to thank the Distinguished Scientist Fellowship Program (DSFP) of King Saud University, Riyadh, Saudi Arabia.

## REFERENCES

- (1) Snaith, H. J. Perovskites: The Emergence of a New Era for Low-Cost, High-Efficiency Solar Cells. *J. Phys. Chem. Lett.* **2013**, *4* (21), 3623–3630.
- (2) Bian, Z.; Wang, Z.; Jiang, B.; Hongmanorom, P.; Zhong, W.; Kawi, S. A Review on Perovskite Catalysts for Reforming of Methane to Hydrogen Production. *Renewable Sustainable Energy Rev.* **2020**, *134*, 110291.
- (3) Umari, P.; Mosconi, E.; De Angelis, F. Relativistic GW Calculations on  $\text{CH}_3\text{NH}_3\text{PbI}_3$  and  $\text{CH}_3\text{NH}_3\text{SnI}_3$  Perovskites for Solar Cell Applications. *Sci. Rep.* **2015**, *4*, 4467.
- (4) Stranks, S. D.; Eperon, G. E.; Grancini, G.; Menelaou, C.; Alcocer, M. J. P.; Leijtens, T.; Herz, L. M.; Petrozza, A.; Snaith, H. J. Electron-Hole Diffusion Lengths Exceeding 1 Micrometer in an Organometal Trihalide Perovskite Absorber. *Science* **2013**, *342* (6156), 341–344.
- (5) Johnston, M. B.; Herz, L. M. Hybrid Perovskites for Photovoltaics: Charge-Carrier Recombination, Diffusion, and Radiative Efficiencies. *Acc. Chem. Res.* **2016**, *49* (1), 146–154.
- (6) Jung, M.; Ji, S.-G.; Kim, G.; Seok, S. I. Perovskite Precursor Solution Chemistry: From Fundamentals to Photovoltaic Applications. *Chem. Soc. Rev.* **2019**, *48* (7), 2011–2038.
- (7) Jeong, J.; Kim, M.; Seo, J.; Lu, H.; Ahlawat, P.; Mishra, A.; Yang, Y.; Hope, M. A.; Eickemeyer, F. T.; Kim, M.; Yoon, Y. J.; Choi, I. W.; Darwich, B. P.; Choi, S. J.; Jo, Y.; Lee, J. H.; Walker, B.; Zakeeruddin, S. M.; Emsley, L.; Rothlisberger, U.; Hagfeldt, A.; Kim, D. S.; Grätzel, M.; Kim, J. Y. Pseudo-Halide Anion Engineering for  $\alpha$ -FAPbI<sub>3</sub> Perovskite Solar Cells. *Nature* **2021**, *592* (7854), 381–385.
- (8) Li, J.; Cao, H.-L.; Jiao, W.-B.; Wang, Q.; Wei, M.; Cantone, I.; Lü, J.; Abate, A. Biological Impact of Lead from Halide Perovskites Reveals the Risk of Introducing a Safe Threshold. *Nat. Commun.* **2020**, *11* (1), 310.
- (9) Schileo, G.; Grancini, G. Lead or No Lead? Availability, Toxicity, Sustainability and Environmental Impact of Lead-Free Perovskite Solar Cells. *J. Mater. Chem. C* **2021**, *9* (1), 67–76.
- (10) Di Girolamo, D.; Pascual, J.; Aldamasy, M. H.; Iqbal, Z.; Li, G.; Radicchi, E.; Li, M.; Turren-Cruz, S.-H.; Nasti, G.; Dallmann, A.; De Angelis, F.; Abate, A. Solvents for Processing Stable Tin Halide Perovskites. *ACS Energy Lett.* **2021**, *6*, 959–968.
- (11) Hao, F.; Stoumpos, C. C.; Cao, D. H.; Chang, R. P. H.; Kanatzidis, M. G. Lead-Free Solid-State Organic–Inorganic Halide Perovskite Solar Cells. *Nat. Photonics* **2014**, *8* (6), 489–494.
- (12) Nasti, G.; Abate, A. Tin Halide Perovskite (ASnX<sub>3</sub>) Solar Cells: A Comprehensive Guide toward the Highest Power Conversion Efficiency. *Adv. Energy Mater.* **2020**, *10* (13), 1902467.
- (13) Jiang, X.; Li, H.; Zhou, Q.; Wei, Q.; Wei, M.; Jiang, L.; Wang, Z.; Peng, Z.; Wang, F.; Zang, Z.; Xu, K.; Hou, Y.; Teale, S.; Zhou, W.; Si, R.; Gao, X.; Sargent, E. H.; Ning, Z. One-Step Synthesis of SnI<sub>2</sub>-(DMSO)<sub>x</sub> Adducts for High-Performance Tin Perovskite Solar Cells. *J. Am. Chem. Soc.* **2021**, *143* (29), 10970–10976.
- (14) Lin, R.; Xiao, K.; Qin, Z.; Han, Q.; Zhang, C.; Wei, M.; Saidaminov, M. I.; Gao, Y.; Xu, J.; Xiao, M.; Li, A.; Zhu, J.; Sargent, E. H.; Tan, H. Monolithic All-Perovskite Tandem Solar Cells with 24.8% Efficiency Exploiting Comproportionation to Suppress Sn(II) Oxidation in Precursor Ink. *Nat. Energy* **2019**, *4* (10), 864–873.
- (15) Yang, Z.; Yu, Z.; Wei, H.; Xiao, X.; Ni, Z.; Chen, B.; Deng, Y.; Habisreutinger, S. N.; Chen, X.; Wang, K.; Zhao, J.; Rudd, P. N.; Berry, J. J.; Beard, M. C.; Huang, J. Enhancing Electron Diffusion Length in Narrow-Bandgap Perovskites for Efficient Monolithic Perovskite Tandem Solar Cells. *Nat. Commun.* **2019**, *10* (1), 4498.
- (16) Li, C.; Song, Z.; Chen, C.; Xiao, C.; Subedi, B.; Harvey, S. P.; Shrestha, N.; Subedi, K. K.; Chen, L.; Liu, D.; Li, Y.; Kim, Y.-W.; Jiang, C.; Heben, M. J.; Zhao, D.; Ellingson, R. J.; Podraza, N. J.; Al-Jassim, M.; Yan, Y. Low-Bandgap Mixed Tin–Lead Iodide Perovskites with Reduced Methylammonium for Simultaneous Enhancement of Solar Cell Efficiency and Stability. *Nat. Energy* **2020**, *5* (10), 768–776.
- (17) Kapil, G.; Bessho, T.; Maekawa, T.; Baranwal, A. K.; Zhang, Y.; Kamarudin, M. A.; Hirotani, D.; Shen, Q.; Segawa, H.; Hayase, S. Tin-Lead Perovskite Fabricated via Ethylenediamine Interlayer Guides to the Solar Cell Efficiency of 21.74. *Adv. Energy Mater.* **2021**, *11* (25), 2101069.
- (18) Noel, N. K.; Stranks, S. D.; Abate, A.; Wehrenfennig, C.; Guarnera, S.; Haghighirad, A.-A.; Sadhanala, A.; Eperon, G. E.; Pathak, S. K.; Johnston, M. B.; Petrozza, A.; Herz, L. M.; Snaith, H. J. Lead-Free Organic–Inorganic Tin Halide Perovskites for Photovoltaic Applications. *Energy Environ. Sci.* **2014**, *7* (9), 3061–3068.

- (19) Pascual, J.; Nasti, G.; Aldamasy, M. H.; Smith, J. A.; Flatken, M.; Phung, N.; Di Girolamo, D.; Turren-Cruz, S.-H.; Li, M.; Dallmann, A.; Avolio, R.; Abate, A. Origin of Sn(II) Oxidation in Tin Halide Perovskites. *Mater. Adv.* **2020**, *1* (5), 1066–1070.
- (20) Meggiolaro, D.; Ricciarelli, D.; Alasmari, A. A.; Alasmari, F. A. S.; De Angelis, F. Tin versus Lead Redox Chemistry Modulates Charge Trapping and Self-Doping in Tin/Lead Iodide Perovskites. *J. Phys. Chem. Lett.* **2020**, *11* (9), 3546–3556.
- (21) Ricciarelli, D.; Meggiolaro, D.; Ambrosio, F.; De Angelis, F. Instability of Tin Iodide Perovskites: Bulk p-Doping versus Surface Tin Oxidation. *ACS Energy Lett.* **2020**, *5* (9), 2787–2795.
- (22) Ambrosio, F.; Meggiolaro, D.; Almutairi, T. M.; De Angelis, F. Composition-Dependent Struggle between Iodine and Tin Chemistry at the Surface of Mixed Tin/Lead Perovskites. *ACS Energy Lett.* **2021**, *6* (3), 969–976.
- (23) Akbulatov, A. F.; Tsarev, S. A.; Elshobaki, M.; Luchkin, S. Y.; Zhidkov, I. S.; Kurmaev, E. Z.; Aldoshin, S. M.; Stevenson, K. J.; Troshin, P. A. Comparative Intrinsic Thermal and Photochemical Stability of Sn(II) Complex Halides as Next-Generation Materials for Lead-Free Perovskite Solar Cells. *J. Phys. Chem. C* **2019**, *123* (44), 26862–26869.
- (24) Leijtens, T.; Prasanna, R.; Gold-Parker, A.; Toney, M. F.; McGehee, M. D. Mechanism of Tin Oxidation and Stabilization by Lead Substitution in Tin Halide Perovskites. *ACS Energy Lett.* **2017**, *2* (9), 2159–2165.
- (25) Mundt, L. E.; Tong, J.; Palmstrom, A. F.; Dunfield, S. P.; Zhu, K.; Berry, J. J.; Schelhas, L. T.; Ratcliff, E. L. Surface-Activated Corrosion in Tin–Lead Halide Perovskite Solar Cells. *ACS Energy Lett.* **2020**, *5* (11), 3344–3351.
- (26) Mosconi, E.; Azpiroz, J. M.; De Angelis, F. Ab Initio Molecular Dynamics Simulations of Methylammonium Lead Iodide Perovskite Degradation by Water. *Chem. Mater.* **2015**, *27* (13), 4885–4892.
- (27) Zheng, C.; Rubel, O. Unraveling the Water Degradation Mechanism of  $\text{CH}_3\text{NH}_3\text{PbI}_3$ . *J. Phys. Chem. C* **2019**, *123* (32), 19385–19394.
- (28) Koocher, N. Z.; Saldana-Greco, D.; Wang, F.; Liu, S.; Rappe, A. M. Polarization Dependence of Water Adsorption to  $\text{CH}_3\text{NH}_3\text{PbI}_3$  (001) Surfaces. *J. Phys. Chem. Lett.* **2015**, *6* (21), 4371–4378.
- (29) Müller, C.; Glaser, T.; Plogmeyer, M.; Sendner, M.; Döring, S.; Bakulin, A. A.; Brzuska, C.; Scheer, R.; Pshenichnikov, M. S.; Kowalsky, W.; Pucci, A.; Lovrinčić, R. Water Infiltration in Methylammonium Lead Iodide Perovskite: Fast and Inconspicuous. *Chem. Mater.* **2015**, *27* (22), 7835–7841.
- (30) Christians, J. A.; Miranda Herrera, P. A.; Kamat, P. V. Transformation of the Excited State and Photovoltaic Efficiency of  $\text{CH}_3\text{NH}_3\text{PbI}_3$  Perovskite Upon Controlled Exposure to Humidified Air. *J. Am. Chem. Soc.* **2015**, *137* (4), 1530–1538.
- (31) Kakekhani, A.; Katti, R. N.; Rappe, A. M. Water in Hybrid Perovskites: Bulk  $\text{MAPbI}_3$  Degradation via Super-Hydrous State. *APL Mater.* **2019**, *7* (4), 041112.
- (32) Caddeo, C.; Saba, M. I.; Meloni, S.; Filippetti, A.; Mattoni, A. Collective Molecular Mechanisms in the  $\text{CH}_3\text{NH}_3\text{PbI}_3$  Dissolution by Liquid Water. *ACS Nano* **2017**, *11* (9), 9183–9190.
- (33) Kye, Y.-H.; Yu, C.-J.; Jong, U.-G.; Chen, Y.; Walsh, A. Critical Role of Water in Defect Aggregation and Chemical Degradation of Perovskite Solar Cells. *J. Phys. Chem. Lett.* **2018**, *9* (9), 2196–2201.
- (34) Long, R.; Fang, W.; Prezhdo, O. V. Moderate Humidity Delays Electron-Hole Recombination in Hybrid Organic-Inorganic Perovskites: Time-Domain Ab Initio Simulations Rationalize Experiments. *J. Phys. Chem. Lett.* **2016**, *7* (16), 3215–3222.
- (35) Aristidou, N.; Eames, C.; Islam, M. S.; Haque, S. A. Insights into the Increased Degradation Rate of  $\text{CH}_3\text{NH}_3\text{PbI}_3$  Solar Cells in Combined Water and  $\text{O}_2$  Environments. *J. Mater. Chem. A* **2017**, *5* (48), 25469–25475.
- (36) Peng, C.; Chen, J.; Wang, H.; Hu, P. First-Principles Insight into the Degradation Mechanism of  $\text{CH}_3\text{NH}_3\text{PbI}_3$  Perovskite: Light-Induced Defect Formation and Water Dissociation. *J. Phys. Chem. C* **2018**, *122* (48), 27340–27349.
- (37) Zhang, L.; Sit, P. H.-L. Ab Initio Study of Interaction of Water, Hydroxyl Radicals, and Hydroxide Ions with  $\text{CH}_3\text{NH}_3\text{PbI}_3$  and  $\text{CH}_3\text{NH}_3\text{PbBr}_3$  Surfaces. *J. Phys. Chem. C* **2015**, *119* (39), 22370–22378.
- (38) Aziz, A.; Aristidou, N.; Bu, X.; Westbrook, R. J. E.; Haque, S. A.; Islam, M. S. Understanding the Enhanced Stability of Bromide Substitution in Lead Iodide Perovskites. *Chem. Mater.* **2020**, *32* (1), 400–409.
- (39) Lanzetta, L.; Webb, T.; Zibouche, N.; Liang, X.; Ding, D.; Min, G.; Westbrook, R. J. E.; Gaggio, B.; Macdonald, T. J.; Islam, M. S.; Haque, S. A. Degradation Mechanism of Hybrid Tin-Based Perovskite Solar Cells and the Critical Role of Tin (IV) Iodide. *Nat. Commun.* **2021**, *12* (1), 2853.
- (40) Lanzetta, L.; Aristidou, N.; Haque, S. A. Stability of Lead and Tin Halide Perovskites: The Link between Defects and Degradation. *J. Phys. Chem. Lett.* **2020**, *11* (2), 574–585.
- (41) Xie, G.; Xu, L.; Sun, L.; Xiong, Y.; Wu, P.; Hu, B. Insight into the Reaction Mechanism of Water, Oxygen and Nitrogen Molecules on a Tin Iodide Perovskite Surface. *J. Mater. Chem. A* **2019**, *7* (10), 5779–5793.
- (42) Kachmar, A.; Berdiyrov, G.; Madjet, M. E.-A. Effect of Water on the Structural, Optical, and Hot-Carrier Cooling Properties of the Perovskite Material  $\text{MASnI}_3$ . *J. Phys. Chem. C* **2019**, *123* (7), 4056–4063.
- (43) Park, C.; Choi, J.; Min, J.; Cho, K. Suppression of Oxidative Degradation of Tin–Lead Hybrid Organometal Halide Perovskite Solar Cells by Ag Doping. *ACS Energy Lett.* **2020**, *5* (10), 3285–3294.
- (44) Kamarudin, M. A.; Hirotani, D.; Wang, Z.; Hamada, K.; Nishimura, K.; Shen, Q.; Toyoda, T.; Iikubo, S.; Minemoto, T.; Yoshino, K.; Hayase, S. Suppression of Charge Carrier Recombination in Lead-Free Tin Halide Perovskite via Lewis Base Post-treatment. *J. Phys. Chem. Lett.* **2019**, *10* (17), 5277–5283.
- (45) Mahata, A.; Meggiolaro, D.; Gregori, L.; De Angelis, F. Suppression of Tin Oxidation by 3D/2D Perovskite Interfacing. *J. Phys. Chem. C* **2021**, *125* (20), 10901–10908.
- (46) Romani, L.; Speltini, A.; Ambrosio, F.; Mosconi, E.; Profumo, A.; Marelli, M.; Margadonna, S.; Milella, A.; Fracassi, F.; Listorti, A.; De Angelis, F.; Malavasi, L. Water-Stable  $\text{DMASnBr}_3$  Lead-Free Perovskite for Effective Solar-Driven Photocatalysis. *Angew. Chem., Int. Ed.* **2021**, *60* (7), 3611–3618.
- (47) Haruyama, J.; Sodeyama, K.; Han, L.; Tateyama, Y. Termination Dependence of Tetragonal  $\text{CH}_3\text{NH}_3\text{PbI}_3$  Surfaces for Perovskite Solar Cells. *J. Phys. Chem. Lett.* **2014**, *5* (16), 2903–2909.
- (48) Li, Q.; Chen, Z.; Tranca, I.; Gaastra-Nede, S.; Smeulders, D.; Tao, S. Compositional Effect on Water Adsorption on Metal Halide Perovskites. *Appl. Surf. Sci.* **2021**, *538*, 148058.
- (49) Weller, M. T.; Weber, O. J.; Henry, P. F.; Di Pumpo, A. M.; Hansen, T. C. Complete Structure and Cation Orientation in the Perovskite Photovoltaic Methylammonium Lead Iodide Between 100 and 352 K. *Chem. Commun.* **2015**, *51* (20), 4180–4183.
- (50) Pisanu, A.; Speltini, A.; Quadrelli, P.; Drera, G.; Sangaletti, L.; Malavasi, L. Enhanced Air-Stability of Sn-Based Hybrid Perovskites Induced by Dimethylammonium (DMA): Synthesis, Characterization, Aging and Hydrogen Photogeneration of the  $\text{MA}_{1-x}\text{DMA}_x\text{SnBr}_3$  System. *J. Mater. Chem. C* **2019**, *7* (23), 7020–7026.
- (51) Pisanu, A.; Mahata, A.; Mosconi, E.; Patrini, M.; Quadrelli, P.; Milanese, C.; De Angelis, F.; Malavasi, L. Exploring the Limits of Three-Dimensional Perovskites: The Case of  $\text{FAPb}_{1-x}\text{Sn}_x\text{Br}_3$ . *ACS Energy Lett.* **2018**, *3* (6), 1353–1359.
- (52) Stoumpos, C. C.; Malliakas, C. D.; Kanatzidis, M. G. Semiconducting Tin and Lead Iodide Perovskites with Organic Cations: Phase Transitions, High Mobilities, and Near-Infrared Photoluminescent Properties. *Inorg. Chem.* **2013**, *52* (15), 9019–9038.
- (53) Hutter, J.; Iannuzzi, M.; Schiffmann, F.; VandeVondele, J. CP2K: Atomistic Simulations of Condensed Matter Systems. *WIREs Comput. Mol. Sci.* **2014**, *4* (1), 15–25.



(54) Kühne, T. D.; Iannuzzi, M.; Del Ben, M.; Rybkin, V. V.; Seewald, P.; Stein, F.; Laino, T.; Khaliullin, R. Z.; Schütt, O.; Schiffmann, F.; Golze, D.; Wilhelm, J.; Chulkov, S.; Bani-Hashemian, M. H.; Weber, V.; Borstnik, U.; Taillefumier, M.; Jakobovits, A. S.; Lazzaro, A.; Pabst, H.; Müller, T.; Schade, R.; Guidon, M.; Andermatt, S.; Holmberg, N.; Schenter, G. K.; Hehn, A.; Bussy, A.; Belleflamme, F.; Tabacchi, G.; Glöß, A.; Lass, M.; Bethune, I.; Mundy, C. J.; Plessl, C.; Watkins, M.; VandeVondele, J.; Krack, M.; Hutter, J. CP2K: An Electronic Structure and Molecular Dynamics Software Package - Quickstep: Efficient and Accurate Electronic Structure Calculations. *J. Chem. Phys.* **2020**, *152* (19), 194103.

(55) VandeVondele, J.; Krack, M.; Mohamed, F.; Parrinello, M.; Chassaing, T.; Hutter, J. Quickstep: Fast and Accurate Density Functional Calculations Using a Mixed Gaussian and Plane Waves Approach. *Comput. Phys. Commun.* **2005**, *167* (2), 103–128.

(56) Kaiser, W.; Carignano, M.; Althman, A. A.; Mosconi, E.; Kachmar, A.; Goddard, W. A.; De Angelis, F. First-Principles Molecular Dynamics in Metal-Halide Perovskites: Contrasting Generalized Gradient Approximation and Hybrid Functionals. *J. Phys. Chem. Lett.* **2021**, *12* (49), 11886–11893.

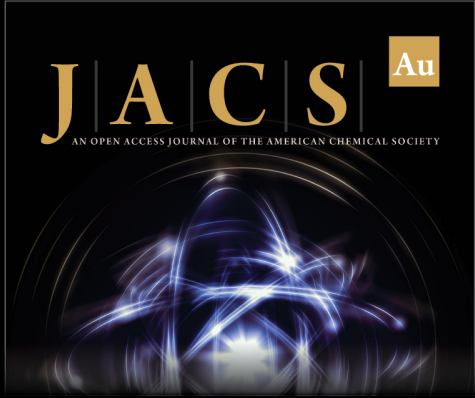
(57) VandeVondele, J.; Hutter, J. Gaussian Basis Sets for Accurate Calculations on Molecular Systems in Gas and Condensed Phases. *J. Chem. Phys.* **2007**, *127* (11), 114105.

(58) Goedecker, S.; Teter, M.; Hutter, J. Separable Dual-Space Gaussian Pseudopotentials. *Phys. Rev. B* **1996**, *54* (3), 1703–1710.


(59) Vydrov, O. A.; van Voorhis, T. Nonlocal van der Waals Density Functional: The Simpler the Better. *J. Chem. Phys.* **2010**, *133* (24), 244103.


(60) Nosé, S. A Unified Formulation of the Constant Temperature Molecular Dynamics Methods. *J. Chem. Phys.* **1984**, *81* (1), 511–519.


(61) Hoover, W. G. Constant-Pressure Equations of Motion. *Phys. Rev. A* **1986**, *34* (3), 2499–2500.



**JACS** Au  
AN OPEN ACCESS JOURNAL OF THE AMERICAN CHEMICAL SOCIETY

 Editor-in-Chief  
**Prof. Christopher W. Jones**  
Georgia Institute of Technology, USA

**Open for Submissions** 

pubs.acs.org/jacsau  ACS Publications  
Most Trusted. Most Cited. Most Read.